Low work-function thermionic emission and orbital-motion-limited ion collection at bare-tether cathodic contact

Xin Chen[1, a)] and J.R. Sanmartín[1, b)]
*Departamento de Física Aplicada, Escuela Técnica Superior de Ingenieros Aeronáuticos,
Universidad Politécnica de Madrid, Plaza Cardenal Cisneros 3, 28040 Madrid,
España.*

(Dated: 28 March 2015)

With a thin coating of low-work-function material, thermionic emission in the cathodic segment of bare tethers might be much greater than orbital-motion-limited (OML) ion collection current. The space charge of the emitted electrons decreases the electric field that accelerates them outwards, or even reverses it for high enough emission, producing a potential valley. In this work, at the conditions of high bias and relatively low emission that make the potential monotonic, an asymptotic analysis is carried out, extending the OML ion-collection analysis to investigate the probe response due to electrons emitted by the negatively-biased cylindrical probe. At given emission, the space charge effect from emitted electrons increases with decreasing magnitude of negative probe bias. Although emitted electrons present negligible space charge far away from the probe, their effect can not be neglected in the global analysis for the sheath structure and two thin layers in between sheath and the quasineutral region. The space-charge-limited (SCL) condition is located. It is found that thermionic emission increases the range of probe radius for OML validity and is greatly more effective than ion collection for cathodic contact of tethers.

I. INTRODUCTION

Electrodynamic tethers are conductive wires allowing flow of electric current between the ends. Arising from the relative motion between plasma and tether in the presence of a planetary magnetic field, a current is induced to flow inside the tether and the magnetic field exerts a force on this current. The tether system exchanges momentum with a planetary magnetosphere and offers the opportunity for in-orbit “propellantless” propulsion around planets with a magnetic field and an ionosphere. Bare (uninsulated) tethers eliminated the need for an electron collector at the anodic end[1–3]. Possibly using bare tethers with no recourse to a plasma contactor at the cathodic end carries the bare-tether concept to its full completion. However, actual ion collection along a cathodic segment is a poor replacement for a hollow cathode. Thermionic emission from materials with low work function (W) may be a good replacement.

A low work function material, $\mathrm{C12A7:e^-}$, was developed and studied at the University of Tokyo by the Prof. H. Hosono's group. In vacuum, $\mathrm{C12A7:e^-}$ electride was found to have a high potential for cold-cathode electron emission. The field-emission characteristics give an extremely low W value, ca. 0.6eV.[4] However, this electride surface easily reacts with O_2 and/or H_2O molecules in the atmosphere, which strongly suggests that an insulating or semiconducting layer inevitably develops on the electric surface. It is thus difficult to prepare a pure intrinsic surface to know an intrinsic work function value[5]. In a later study, a value for W was found to be somewhat higher, ca. 2.4eV, although it was still very low[6]. Recent study in Colorado State University gave a value of 0.76eV.[7] In tether applications, we can expect a low work function due to low density of air molecules in space. Considering the lowest value found 0.6eV, it can emit intense current ($10\mathrm{A/m^2}$) at temperature about 300K, well below values (1200K – 1300K) required by state-of-art electron emitting materials, say, LaB6 and CeB6 (2.7eV). Another feature of interest of $\mathrm{C12A7:e^-}$ electride is its high thermal stability compared to state-of-art materials. Coating a tether with $\mathrm{C12A7:e^-}$ would allow efficient thermionic emission, and so cathodic contact, at reasonable working temperatures[8,9].

Thermionic emission is different from hollow cathode emission in important respects concerning a tether system:

- Only electrons rather than plasma are emitted
- Cylindrical rather than spherical geometry is involved, which allows for collected ion current to follow an explicit law
- A relatively definite physical law for emission current is involved, which is not the case for a hollow cathode, for which broadly different regimes may exist, giving rise to quite different schemes/analyses
- Thermionic emission allows the current to be emitted over a long segment of tether under a range of voltage-bias values, other than being emitted only at tether end as with hollow cathodes
- Use of laboratory test results in designing HC for generic use in space is tricky.

In the case of no emission, current collection and sheath structure around a spherical Langmuir probe have been studied in the literature, using orbital-motion

---

[a)] Electronic mail: xin.chen@upm.es
[b)] Electronic mail: juanr.sanmartin@upm.es

theory for mono-energetic attracted species[10–12], while the cylindrical case was investigated for a Maxwellian distribution[13–16]. The impact of relativistic effects using similar methods has been analyzed for a possible Jupiter mission with electrodynamic bare tethers[17,18]. The effects of emission were first investigated by Langmuir for a planar sheath problem, not fully self-consistent but a good approximation for strong double layers[19]. Fluid models have then been often used in the literature to analyze planar[20–22], cylindrical[23] or spherical[24] sheath structures. Following orbital-motion theory, Chang and Bienkowski discussed the electron emission effects in front of spherical and cylindrical probes, considering their kinetics and the attracted species as mono-energetic[25].

This study, following closely the methods in Ref. 14, extends the orbital-motion-limited (OML) ion-collection analysis to investigate the probe response due to electrons emitted by the negatively-biased cylindrical probe. Sections II and III formulate and model the problem of thermionic emission in the bare-tether application. In Sec. IV we compute the maximum probe radius-to-Debye length ratio R_{max}/λ_D for the OML regime to hold, and also locate the space-charge-limited (SCL) condition, for which the electric field vanishes at the probe, as result from the space charge arising from emitted electrons. Results are discussed in Sec. V.

II. BARE TETHER WITH THERMIONIC EMISSION

A bare tether collects (electron collection) and emits (ion collection or electron emission) current, along the anodic segment AB ($\Phi_p > 0$) and the cathodic segment BC ($\Phi_p < 0$) respectively (Fig. 1). The current flowing along the tether vanishes at both ends. The small cross-sectional dimension and the kilometers-long length of the tether allow each point on the cathodic segment to emit current as if it were part of a cylindrical probe uniformly polarized at the local tether bias $\Phi_p < 0$, under two-dimensional probe conditions that are also applied to the anodic-segment analysis.

In an unmagnetized plasma at rest, Poisson's equation governing the electrostatic potential

$$\frac{1}{r}\frac{\mathrm{d}}{\mathrm{d}r}\left(r\frac{\mathrm{d}\Phi}{\mathrm{d}r}\right) = \frac{e}{\varepsilon_o}(N_e + N_{em} - N_i)\ , \qquad (1)$$

presents axial symmetry with boundary conditions $\Phi = \Phi_p$ at $r = R$, $\Phi \to 0$ as $r \to \infty$. This is to be supplemented by equations for number densities of ambient plasma ions N_i and electrons N_e, and emitted electrons N_{em}.

As in the case of no emission and a collisionless plasma, under high bias assumption, ions arrive at the negatively biased probe as electrons arriving at the positively biased probe in Ref. 14; thus, N_i and N_e can be calculated by the same kinetic analysis of the particle trajectories. The Vlasov equation conserves the distribution function of plasma ions along their orbits, being an undisturbed Maxwellian distribution at infinity. Due to the high negative bias, the repelled plasma electron density is approximated by the simple Boltzmann law,

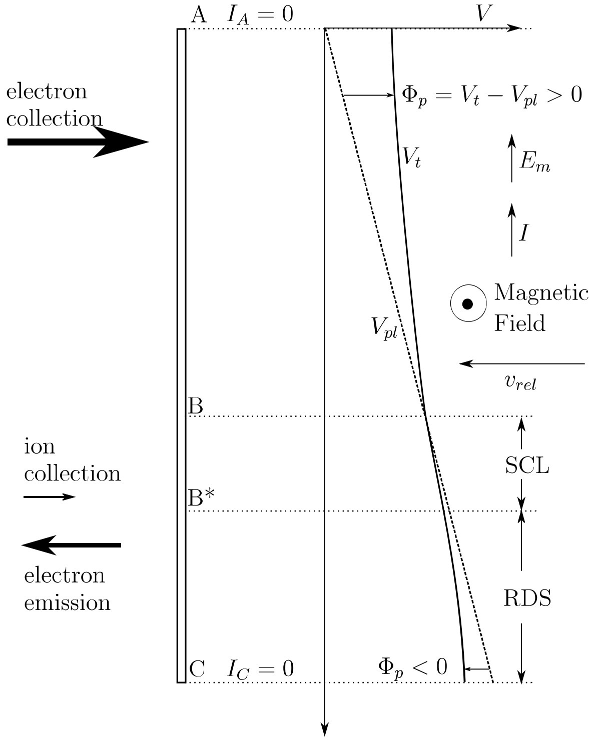

FIG. 1. Scheme of tether-to-plasma potential Φ_p, tether potential V_t, plasma potential V_{pl} and current I along a floating bare tether, operating in drag mode. E_m is the motional electric field, and v_{rel} is tether velocity relative to ambient plasma.

$$\frac{N_e(r)}{N_\infty} = \exp\left[\frac{e\Phi(r)}{kT_e}\right]\ , \qquad (2)$$

where N_∞ is the electron and ion particle density at infinity. Asymptotic analysis of Poisson's equation had been carried out from infinity to the probe, crossing regions with different behaviors, at the particular condition $R = R_{max}$ and beyond $R > R_{max}$, and high bias[14,15]. R_{max} is the largest radius for the OML regime to hold, the current being maximum as[14],

$$I_{i,eOML} \approx 2RLeN_\infty\sqrt{\frac{2|e\Phi_p|}{m_{i,e}}}\ , \qquad (3)$$

where R and L are probe radius and length respectively. Plotting the potential profile $\Phi(r)/\Phi_p$ against R^2/r^2 (Fig. 2, as Fig. 2 in Ref. 14), the curve lies entirely above the diagonal in case of OML regime ($R \le R_{max}$, $I_i = I_{iOML}$), otherwise the non-OML regime ($R > R_{max}$, $I_i < I_{iOML}$) applies[15,16].

In the presence of emission, emitted electrons result in negative space charge, which decreases the electric field that accelerates them outwards, or even reverses it, decelerating electrons near the emitting probe. In the case of a

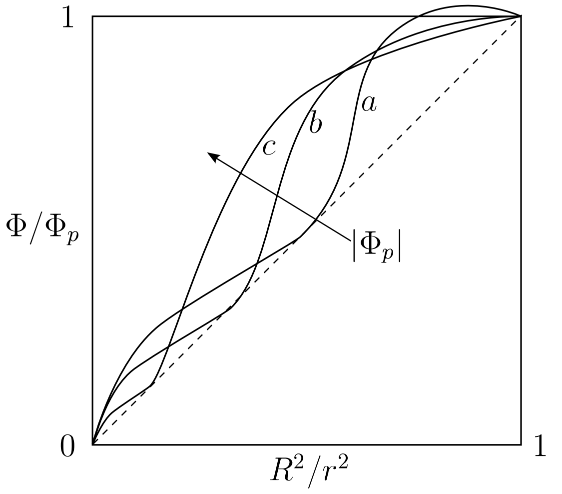

FIG. 2. Schematics of potential profile Φ/Φ_p versus R^2/r^2 for given emission, $R = R_{max}$, and different bias values.

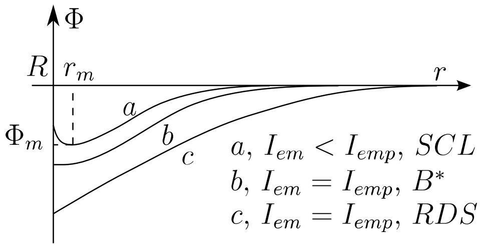

FIG. 3. Typical potential distributions of a negatively biased probe in the presence of electron emission.

monotonic potential as curve c in Fig. 3, all electrons are accelerated outwards without meeting any barrier, corresponding to the emission at any local point on segment CB* (Fig. 1). Considering the cathodic segment coated with a material having work function W, the emitted current I_{em} at this segment is as high as the maximum current that can possibly be emitted by the probe I_{emp}, given by the Richardson-Dushman (RDS) equation,

$$I_{emp} = 2\pi RLC \times T_p^2 \exp\left(-\frac{W}{kT_p}\right) ,$$
$$C = \frac{4\pi m_e k^2 e}{h^3} = 1.2017 \times 10^6 \mathrm{A}/m^2\mathrm{K}^{\ 2}, \qquad (4)$$

as function of W and probe temperature T_p, being independent of bias. As $|\Phi_p|$ decreases from tether end C, negative space charge increases its effect, and at some point B*, the electric field vanishes at the probe (curve b in Fig. 3), which is the onset of current being SCL. In Fig. 2, curve b is horizontal at the probe surface $R^2/r^2 = 1$. Under further decrease of $|\Phi_p|$ from B* to zero-bias-point B, a potential valley develops in front of the tether (curve a in Fig. 3). The resultant local minimum Φ_m repels electrons not energetic enough back to the probe, the current being $I_{em} < I_{emp}$. In Fig. 2, curve a would then actually exceed the full square frame.

In this work, we concentrate on the no-valley, monotonic potential case, corresponding to the segment B*C in Fig. 1. Under assumptions of high bias and relatively low emission, emitted electrons are accelerated across the sheath, presenting a small amount of space charge in the quasineutral region far away from the probe. Outside but close to the sheath, the behavior of the potential profile would be similar to that of non-emitting OML ion collection, with modifications arising from the space charge of emitted electrons, in particular on the two transitional layers that match the quasineutral and sheath regions. For simplicity, we consider throughout $R = R_{max}$ cases, where potential profile curves in Fig. 2 are tangent to the diagonal at some radius r in the quasineutral region. Considering equal plasma electron-ion temperature $T_e = T_i = T$, we look for the general parametric dependence of R_{max} and locate the probe bias where the current starts to be SCL (curve b in Figs. 2 and 3).

III. MODELLING

In absence of collisions, particles describe free orbits in the axially symmetric potential field. The condition for a particle to reach the probe can then be derived from simple mechanical conservation laws. In a central force field where cylindrical symmetry prevails, two constants of motion, in addition to the axial velocity, characterize the particle orbit, being transverse energy E and angular momentum J.

For ions, E and J are

$$E = \frac{m_i v_r^2}{2} + \frac{m_i v_\theta^2}{2} + e\Phi(r) \ , \quad J = m_i r v_\theta \ , \qquad (5)$$

with E positive because $\Phi_\infty = 0$ but J covering both positive and negative values. For an ion with energy E to possibly exist at r, its J has to satisfy the cutoff boundary[13],

$$J^2 - J_r^2(E) = -m_i^2 r^2 v_r^2 \leq 0 \ ,$$
$$J_r^2(E) = 2m_i r^2 (E - e\Phi) \ . \qquad (6)$$

Actually, for an ion with energy E to arrive at r from infinity, its angular momentum must satisfy the cutoff boundary everywhere beyond r, which is called the absorption boundary,

$$J^2 \leq J_r^{*2}(E) = \min\{J_{r'}^2(E) : r' \geq r\} \ . \qquad (7)$$

At radius r, for incoming ions with energy E, the momentum range is $J^2 \leq J_r^{*2}(E)$. Among these ions, those with $J^2 < J_R^{*2}(E)$ arrive and disappear at the probe, leaving the rest reflected back to r. Thus the outgoing ions at r have the momentum range as $J_R^{*2}(E) \leq J^2 \leq J_r^{*2}(E)$. After integration of the undisturbed Maxwellian distribution function over the energy domain $E \geq 0$ and the corresponding J domain for both incoming and outgoing

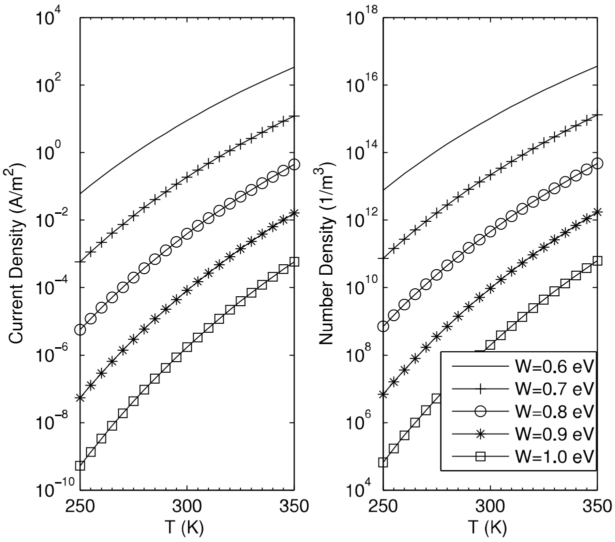

FIG. 4. Richardson-Dushman current density and emitted particle density versus probe temperature for different work function of the emitting material.

ions, the ion density at r becomes[14]

$$\frac{N_i(r)}{N_\infty} = \int_0^\infty \frac{\exp(-E/kT)}{\pi kT} \times \left[2 \times \arcsin \frac{J_r^*(E)}{J_r(E)} - \arcsin \frac{J_R^*(E)}{J_r(E)} \right] \mathrm{d}E \ , \quad (8)$$

where $J_R^*(E) = J_R(E)$ in the case of $R \leq R_{max}$, and $J_r(E) \geq 0$ is chosen for simplicity of presentation.

Electrons are emitted at the probe with a half-Maxwellian velocity distribution[25,26],

$$f_{em}(R, v_r, v_\theta) = \frac{N_{emp} m_e}{\pi k T_p} \exp\left(-\frac{m_e {v_r}^2/2 + m_e {v_\theta}^2/2}{kT_p} \right) \ , \quad (9)$$

N_{emp} can thus be associated with I_{emp} as

$$N_{emp} = \frac{I_{emp}/2\pi RL}{e\sqrt{2kT_p/\pi m_e}} \ . \quad (10)$$

The emitted current density and particle density versus probe temperature for different work function are shown in Fig. 4. The Vlasov equation conserves the distribution function along electron orbits. Since we consider the case of monotonic potential, v_θ decreases as angular momentum

$$J_e = m_e r v_\theta \quad (11)$$

keeps constant while moving outwards. Radial velocity thus increases, as energy

$$E_e = m_e v_r^2/2 + m_e v_\theta^2/2 - e\Delta\phi \ , \quad \Delta\Phi = \Phi - \Phi_p \ , \quad (12)$$

keeps constant too, v_θ decreases, and Φ increases. As a result, there is no potential barrier and all electrons emitted at the probe can reach infinity and are thus present at any r. For electrons with energy E_e, the integration domain of J_e is thus

$$0 \leq J_e^2 \leq J_{eR}^2(E_e) = 2m_e R^2 E_e \ , \quad (13)$$

where we defined $J_{er}^2 = 2m_e r^2(E_e + e\Delta\Phi)$. The velocity distribution integration becomes

$$\frac{N_{em}(r)}{N_{emp}} = 2\int_0^\infty \frac{\exp(-E_e/kT_p)}{\pi k T_p} \times \arcsin\sqrt{\frac{R^2 E_e}{r^2(E_e + e\Delta\Phi)}} \, \mathrm{d}E_e \ . \quad (14)$$

Taylor expansion of $\arcsin\sqrt{a^2x/(x+1)}$ around $x \to 0$ is $\arcsin\sqrt{a^2x/(x+1)} = a\left(\sqrt{x} + O[x]^{3/2}\right)$. Under condition of $e\Delta\Phi/kT_p \gg 1$, we have

$$\arcsin\sqrt{\frac{R^2 E_e}{r^2(E_e + e\Delta\Phi)}} = \frac{R}{r}\left\{ \sqrt{\frac{E_e}{e\Delta\Phi}} + O\left(\left[\frac{E_e}{e\Delta\Phi} \right]^{3/2} \right) \right\} \ . \quad (15)$$

The emitted electron density becomes

$$\frac{N_{em}(r)}{N_{emp}} \approx \frac{R}{r}\sqrt{\frac{kT_p}{\pi e(\Phi - \Phi_p)}} \ , \quad (16)$$

which corresponds to radial motion away from the probe. This approximation has an error of the order of $[kT_p/e\Delta\Phi]^{3/2}$, breaking down near the probe surface where the error becomes infinite. However, the conditions of high bias and low probe temperature (low energy of emitted electrons) confine the failure of this approximation to the vicinity of the probe.

We introduce normalized quantities as

$$\xi_D = \frac{R}{\lambda_D} \ , \quad \nu = \frac{N_{emp}}{N_\infty} \ , \quad \theta = \frac{T}{T_p} \ ,$$

$$z = \frac{r}{R} \ , \quad \Psi(z) = -\frac{e\Phi(r)}{kT_e} > 0 \ , \quad (17)$$

$$n_{i,e}(z) = \frac{N_{i,e}(r)}{N_\infty} \ , \quad n_{em}(z) = \frac{N_{em}(r)}{N_{emp}} \ , \quad (18)$$

$$\epsilon = \frac{E}{kT_i} \ , \quad j_z^2(\epsilon) = \frac{J_r^2}{2m_i R^2 kT_i} = z^2(\epsilon + \Psi) \ . \quad (19)$$

Then Poisson's equation becomes

$$\frac{1}{\xi_D^2 z}\frac{\mathrm{d}}{\mathrm{d}z}\left(z\frac{\mathrm{d}\Psi}{\mathrm{d}z} \right) = n_i - n_e - \nu n_{em} \ , \quad (20)$$

$$\Psi(1) = \Psi_p > 0 \ , \quad \Psi(\infty) \to 0 \ , \quad (21)$$

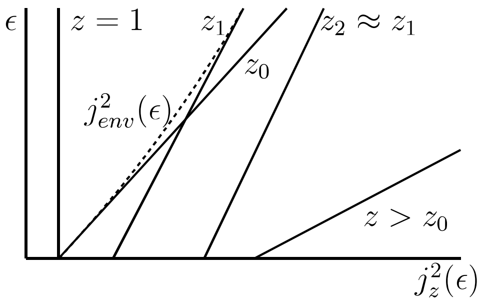

FIG. 5. Straight lines of the z-family lines $j_z^2(\epsilon)$. A high bias assumption implies $\Psi_p \gg \epsilon$ for the values $\epsilon = O(1)$ of interest in the integrations. As a result, the $z = 1$ line has a steep slope in this schematic plot.

where densities are

$$n_i(z) = \int_0^\infty \frac{\exp(-\epsilon)}{\pi} \times \left[2 \times \arcsin\frac{j_z^*(\epsilon)}{j_z(\epsilon)} - \arcsin\frac{\sqrt{\Psi_p}}{j_z(\epsilon)}\right] \mathrm{d}\epsilon \ , \tag{22}$$

$$n_e(z) = \exp(-\Psi) \ , \tag{23}$$

$$n_{em}(z) = \frac{1}{z\sqrt{\pi\theta(\Psi_p - \Psi)}} \ , \tag{24}$$

and the high bias assumption $j^2_{z=1}(\epsilon) \approx \Psi_p$ has been used in Eq. (22). Note that $j_r(\epsilon) \geq 0$ is chosen for simplicity of presentation. The absorption boundary $j_z^{*2}(\epsilon)$ can be illustrated by considering the z-family of straight lines $j_z^2(\epsilon)$ as in Fig. 5, the slopes being $1/z^2$ and x-intercepts being $z^2\Psi$. The change of $z^2\Psi$ follows the ordinate-to-abscissa profile ratio in Fig. 2. The system (20)-(24) must be solved for given values of all the parameters ν, θ, and Ψ_p. Note that the ξ_D value is assumed to be R_{max}/λ_D, which must be determined as part of the solution.

IV. SCL CONDITION AND MAXIMUM RADIUS FOR OML VALIDITY

A. $z > z_0$

As ions moving inwards from infinity, $z^2\Psi$ decreases and the z-line keeps moving to the left for z decreasing for all positive energies (Fig.5). This no barrier condition $j_z^*(\epsilon) = j_z(\epsilon)$ holds until z_0, where $z^2\Psi$ starts to increase. If $R = R_{max}$, z_0 lies on the diagonal in Fig. 2, giving $z_0^2\Psi_0 = \Psi_p$. For $z > z_0$, the ion density in Eq. (22) becomes

$$n_i(z) = 1 - \int_0^\infty \frac{\exp(-\epsilon)}{\pi} \arcsin\sqrt{\frac{\Psi_p}{j_z^2(\epsilon)}} \, \mathrm{d}\epsilon \ . \tag{25}$$

And, due to $\Psi \ll \Psi_p$ in this region, the emitted electron density in Eq. (24) can be approximated as

$$n_{em}(z) \approx \frac{1}{z\sqrt{\pi\theta\Psi_p}} \ . \tag{26}$$

Thus the potential for any $z \geq z_0$ is given by solving the quasineutrality equation

$$1 - \int_0^\infty \frac{\exp(-\epsilon)}{\pi} \arcsin\sqrt{\frac{\Psi_p}{j_z^2(\epsilon)}} \, \mathrm{d}\epsilon - \exp(-\Psi) - \frac{\nu}{z\sqrt{\pi\theta\Psi_p}} = 0 \ . \tag{27}$$

We can thus determine z_0 and Ψ_0 by conditions

$$1 + \exp(\Psi_0)\,\mathrm{erfc}\left(\sqrt{\Psi_0}\right) = 2\exp(-\Psi_0) + \frac{2\nu}{\Psi_p}\sqrt{\frac{\Psi_0}{\pi\theta}} \ , \tag{28}$$

$$\Psi_0 = \Psi_p/z_0^2 \ . \tag{29}$$

Because Eq. (25) is valid as long as $R \leq R_{max}$, the potential profile for $z > z_0$ calculated from Eq. (27) is also valid for $R \leq R_{max}$, being function of ν, θ and Ψ_p only, independent of R. This indicates that Eq. (25) does not result in $\mathrm{d}\left(z^2\Psi\right)/\mathrm{d}z = 0$ at z_0, which is the accurate definition of z_0. Therefore, the position of z_0 can not arise from this approximated quasineutrality solution directly. In this study, we impose the condition $R = R_{max}$ and $z_0^2\Psi_0 = \Psi_p$, acquiring z_0 and Ψ_0 by Eqs. (28) and (29) before the global sheath solution is found. Then looking for the R_{max} value that provides a consistent solution does require a jump of $\mathrm{d}\left(z^2\Psi\right)/\mathrm{d}z$ at z_0. However, using locally the full Poisson's equation Eq. (20) around z_0 and Eqs. (22), (23) and (26) for particle densities can round the profile at z_0, with no effect beyond its immediate neighbourhood[14].

B. $z_1 < z < z_0$

From z_0 inwards, with the quasineutral condition still holding, the no barrier condition does fail as $z^2\Psi$ starts to increase. Quasineutrality itself is found to break down at some point z_1 where $\mathrm{d}\Psi/\mathrm{d}z$ diverges. The knowledge of $\Psi(z)$ itself is required to determine the envelope of the z-lines in $\epsilon - j$ plane, the dashed curve in Fig. 5, and thus to determine $j_z^*(\epsilon)$. We approximate this envelope by a hyperbola that is tangent to the z_0 line at $\epsilon = 0$ and $j_z^2 = z_0^2\Phi_0$, and limited by the z_1 line as the asymptote for $\epsilon \to \infty$[14],

$$j^2_{env}(\epsilon) = j^2_{z_1}(\epsilon) - \frac{(z_1^2\Psi_1 - z_0^2\Psi_0)^2}{z_1^2\Psi_1 - z_0^2\Psi_0 + (z_0^2 - z_1^2)\epsilon} \ . \tag{30}$$

Use of Eq. (30), however, requires values for z_1 and Ψ_1 which are still unknown. Near z_1, we have $j_z^*(\epsilon) \approx$

$j_{env}(\epsilon)$, and thus the ion density becomes

$$n_i(z) = \int_0^\infty \frac{\exp(-\epsilon)}{\pi} \times \left[2 \times \arcsin\frac{j_{env}(\epsilon)}{j_z(\epsilon)} - \arcsin\frac{\sqrt{\Psi_p}}{j_z(\epsilon)}\right] \mathrm{d}\epsilon \ . \tag{31}$$

Use of Eq. (31) for quasineutrality at z_1 provides a first relation for z_1 and Ψ_1. If we write the quasineutrality equation as $f(z, \Psi) = 0$, the implicit function theorem gives $\mathrm{d}f/\mathrm{d}\Psi = \partial f/\partial\Psi + \partial f/\partial z \cdot \mathrm{d}z/\mathrm{d}\Psi = 0$. Another relation thus arises from using the equivalence of the divergent condition $\mathrm{d}z/\mathrm{d}\Psi = 0$ at z_1, rewritten as

$$\left.\frac{\partial n_i(z)}{\partial\Psi}\right|_{z_1} - \left.\frac{\partial n_e(z)}{\partial\Psi}\right|_{z_1} - \left.\frac{\partial n_{em}(z)}{\partial\Psi}\right|_{z_1} = 0 \ , \tag{32}$$

where $\partial n_{em}(z)/\partial\Psi|_{z_1}$ actually vanishes. Thus z_1 and Ψ_1 can be found from equations

$$\int_0^\infty \frac{\exp(-\epsilon)}{\pi} \times \left[2 \times \arcsin\frac{j_{env}(\epsilon)}{j_{z_1}(\epsilon)} - \arcsin\frac{\sqrt{\Psi_p}}{j_{z_1}(\epsilon)}\right] \mathrm{d}\epsilon - \exp(-\Psi_1) - \frac{\nu}{z_1\sqrt{\pi\theta\Psi_p}} = 0 \ , \tag{33}$$

$$\int_0^\infty \frac{\exp(-\epsilon)}{2\pi(\epsilon+\Psi_1)} \times \left[2\sqrt{\frac{j_{env}^2(\epsilon)}{j_{z_1}^2(\epsilon) - j_{env}^2(\epsilon)}} - \sqrt{\frac{\Psi_p}{j_{z_1}^2(\epsilon) - (\epsilon+\Psi_p)}}\right] \mathrm{d}\epsilon - \exp(-\Psi_1) = 0 \ . \tag{34}$$

With the approximated envelope, we can determine $\epsilon_{env}(z)$, where the envelope osculates with the z line at. As the envelope shares the same slope with z line at ϵ_{env}, $\mathrm{d}j_{env}^2(\epsilon)/\mathrm{d}\epsilon|_{\epsilon_{env}} = \mathrm{d}j_z^2(\epsilon)/\mathrm{d}\epsilon|_{\epsilon_{env}} = z^2$ gives

$$\epsilon_{env}(z) = \frac{\sqrt{\frac{(z_1^2\Psi_1 - z_0^2\Psi_0)^2(z_0^2 - z_1^2)}{z^2 - z_1^2}} - (z_1^2\Psi_1 - z_0^2\Psi_0)}{z_0^2 - z_1^2} \ . \tag{35}$$

The relation $j_z(\epsilon_{env}) = j_{env}(\epsilon_{env})$ then directly gives the potential,

$$\Psi(z) = \frac{j_{env}^2(\epsilon_{env})}{z^2} - \epsilon_{env} \ . \tag{36}$$

Note that, once the potential profile is determined throughout, the resultant overall particle density $n_i - n_e - \nu n_{em}$ can be used to evaluate the error of Eq. (30) as $j_{env}(\epsilon)$ approximation. For ion density at any radius between z_0 and z_1, we have in Eq. (22),

$$\begin{aligned} j_z^*(\epsilon) &= j_{env}(\epsilon), \quad \text{for} \quad \epsilon < \epsilon_{env}(z) \\ &= j_z(\epsilon), \quad \text{for} \quad \epsilon \geq \epsilon_{env}(z) \ . \end{aligned} \tag{37}$$

The maximum error evaluated for values $\theta = 4$, $\nu = 0$, 20, 50, 70, and 100 is found of the order of 1% or less, validating that approximation.

C. Two transitional layers

From z_1 inwards, because of the sharp increase in Ψ, quasineutrality breaks down. A very thin transitional layer, in the vicinity of z_1, takes the solution to a radius z_2 a bit closer to the probe, where Ψ, rather than $\mathrm{d}\Psi/\mathrm{d}z$, is found to actually diverge as $\Psi - \Psi_1 \propto (z - z_2)^{-2}$. The structure of the this layer is considered in Appendix A. The location of z_2 is found in Eq. (A6) as

$$z_2 = z_1(1 - \beta\xi_2) \ , \ \xi_2 \approx 3.42 \ , \ \beta \equiv \left(\sqrt{\frac{2}{\lambda\mu}}\frac{1}{\xi_D^2 z_1^2}\right)^{2/5} \ , \tag{38}$$

where λ and μ are defined in Eqs. (A2) and (A3). As different from the determination of z_0, z_1, Ψ_0 and Ψ_1, the value of z_2, which depends on ξ_D appearing in β, can not be calculated until the entire sheath structure is solved. If ξ_D is somehow poorly determined, the same applies to z_2.

A second thin transitional layer around z_2 is needed to match the solution inside the sheath. At this layer, being thin and faraway from the probe under high bias assumption, space curvature can be ignored in 2D Laplace operator of Poisson's equation, equivalently $z \approx z_2$. In this layer however, the complete expression of the RHS of Poisson's equation needs to be retained as:

$$\frac{\mathrm{d}^2\Psi}{\xi_D^2\,\mathrm{d}z^2} = \int_0^\infty \frac{\exp(-\epsilon)}{\pi}\left[2 \times \arcsin\sqrt{\frac{j_{env}^2(\epsilon)}{z_2^2(\epsilon+\Psi)}} - \arcsin\sqrt{\frac{\Psi_p}{z_2^2(\epsilon+\Psi)}}\right]\mathrm{d}\epsilon - \frac{\nu}{z_2\sqrt{\pi\theta\Psi_p}} \ , \tag{39}$$

where the ambient electrons density has been neglected. To match the first transitional layer, we have the behavior of the potential from z_2 outwards as

$$\Psi = \frac{12}{\lambda\xi_D^2(z_1 - z_1\beta\xi_2 - z)^2} + \Psi_1 \ . \tag{40}$$

From z_2 inwards, to match the sheath at the top of this layer, the sharp increase of Ψ results in $j_z^2(\epsilon) \gg j_{env}(\epsilon)$ and $z_2^2\Psi \gg \epsilon$ for the values $\epsilon = O(1)$ of interest, thus giving the ion density as

$$n_i = \frac{\kappa}{\pi z_2}\sqrt{\frac{\Psi_p}{\Psi}} \ , \tag{41}$$

where κ is

$$\kappa = \int_0^\infty \frac{2\exp(-\epsilon)j_{env}(\epsilon)}{\sqrt{\Psi_p}}\mathrm{d}\epsilon - 1 \ . \tag{42}$$

Poisson's equation becomes

$$\frac{\mathrm{d}^2\Psi}{\xi_D^2\,\mathrm{d}z^2} = \frac{\kappa}{\pi z_2}\sqrt{\frac{\Psi_p}{\Psi}} - \frac{\nu}{z_2\sqrt{\pi\theta\Psi_p}}\ . \tag{43}$$

After changing variables

$$g = g_p\frac{\Psi}{\Psi_p}\ ,\quad g_p = \left(\frac{\pi\Psi_p}{\kappa z_2\xi_D^2}\right)^{2/3}\ ,\quad u = \ln\frac{z_2}{z}\ , \tag{44}$$

Poisson's equation becomes

$$\frac{\mathrm{d}^2 g}{\mathrm{d}u^2} = \frac{1}{\sqrt{g}} - \frac{\mu_s}{\sqrt{g_p}}\ ,\quad \mu_s = \frac{\nu}{\kappa}\sqrt{\frac{\pi}{\theta\Psi_p}}\ , \tag{45}$$

where the $\mathrm{d}z \approx z_2\,\mathrm{d}u$ has been applied. If $\mu_s/\sqrt{g_p}$ is much smaller than $1/\sqrt{g}$, we can assume $g \approx g_0 + g_1$, where $g_1 \ll g_0$ is the correction due to small $\mu_s/\sqrt{g_p}$. Then we have

$$\frac{\mathrm{d}^2 g}{\mathrm{d}u^2} \approx \frac{1}{\sqrt{g_0}} - \frac{g_1}{2g_0^{3/2}} - \frac{\mu_s}{\sqrt{g_p}}\ . \tag{46}$$

After integrating the resultant equations $g_0'' = 1/\sqrt{g_0}$ and $g_1'' = -g_1/2g_0^{3/2} - \mu_s/\sqrt{g_p}$, we find the behavior at inward tip of the second transitional layer for increasing u,

$$g = \left(\frac{3u}{2}\right)^{4/3} - \frac{9\mu_s}{20\sqrt{g_p}}u^2\ . \tag{47}$$

As g becomes large along with u, moving into the sheath, $\mu_s/\sqrt{g_p}$ becomes comparable to $1/\sqrt{g}$, and the two-term expansion in Eq. (47) provides the matching condition for the sheath.

D. Sheath

Inside the sheath, z-lines lie far to the right, leading to $j_{z=1}(0) \ll j_z(\epsilon) \approx j_z(0)$ and $j_z^*(\epsilon) = j_{env}(\epsilon) \sim j_{z=1}(0)$, the ion density then reading

$$n_i(z) = \frac{\kappa}{\pi z}\sqrt{\frac{\Psi_p}{\Psi}}\ , \tag{48}$$

where κ is given by Eq. (42). Although this approximation fails near the probe, as with the approximation Eq. (24), the high bias assumption makes space-charge effects negligible within some neighborhood of the probe. Moreover, in the case of sufficient electron emission, the ion space charge is small compared to that of the emitted electrons and thus the error of this approximation can be further neglected. The plasma electron density can be ignored inside the sheath, and the emitted electron density used is the fluid approximation of Eq. (24). We impose a bound $n_{em} = 1$ if $n_{em} > 1$. Poisson's equation now becomes

$$\frac{1}{z\xi_D^2}\left(\frac{\mathrm{d}}{\mathrm{d}z}z\frac{\mathrm{d}\Psi}{\mathrm{d}z}\right) = \frac{\kappa}{\pi z}\sqrt{\frac{\Psi_p}{\Psi}} - \frac{\nu}{z\sqrt{\pi\theta\left(\Psi_p - \Psi\right)}}\ . \tag{49}$$

Using same changes of variables as Eq. (44) yields Poisson's equation as

$$\frac{\mathrm{d}^2 g}{\mathrm{d}u^2} = \exp(-u)\left(\frac{1}{\sqrt{g}} - \frac{\mu_s}{\sqrt{g_p - g}}\right)\ . \tag{50}$$

To match with the behavior of the potential at the inward tip of the second transitional layer given by Eq. (47), for small $u > 0$ we have

$$g = \left(\frac{3u}{2}\right)^{4/3} - \frac{9\mu_s u^2}{20\sqrt{g_p}}\ ,\quad g' = (12u)^{1/3} - \frac{9\mu_s u}{10\sqrt{g_p}}\ , \tag{51}$$

where the curvature effect, represented by the factor e^{-u} in Eq. (50), is ignored.

Equation (50) must be integrated from small u, with the behavior of Eq. (51), till reaching the probe at $z = 1$, i.e., $u_p = \ln z_2$. Integration depends on the unknown parameter ξ_D. For given ν, θ, and Ψ_p, the corresponding $\xi_{Dm}(\nu,\theta,\Psi_p) = R_{max}/\lambda_D$ is determined by trial iteration, till condition $g(u_p) = g_p$ is satisfied,

$$g\left[\ln z_2(\xi_{Dm})\right] = \left(\frac{\pi\Psi_p}{z_2\kappa\xi_{Dm}^2}\right)^{2/3}\ . \tag{52}$$

For decreasing values of Ψ_p, the derivative $\mathrm{d}g/\,\mathrm{d}u$ at the probe keeps positive until the SCL condition $\mathrm{d}g/\,\mathrm{d}u = 0$ is reached. The probe potential here, $\Psi_{SCL}(\nu,\theta)$, is the minimum of Ψ_p values that allow monotonic potential profile.

V. RESULTS AND DISCUSSION

Let us discuss the results with some typical data in space, $kT = 0.1$eV and a somewhat low day density $N_\infty = 3\times10^{11}/\mathrm{m}^2$. Results are shown for a tentative tether temperature $\theta = 4$ ($T_p \approx 290.1$K) and several emitted electron densities, $\nu = 20$, 50, 70 and 100, corresponding to work function $W \approx 0.708$, 0.685, 0.677 and 0.668eV respectively.

For different ν values and a range of Ψ_p values, Figure 6 shows R_{max}/λ_D and $\mathrm{d}g/\,\mathrm{d}u|_{z=1}$, Figure 7 shows Ψ_0, Ψ_1, Ψ_p/z_1^2, and Ψ_p/z_2^2, and Figure 8 shows the parameters β, κ, g_p, and μ_s. The results for the case of no emission ($\nu = 0$) are also shown in the figures. Except for the $\nu = 0$ case, the curves end at the probe potential $\Psi_{SCL}(\nu,\theta)$, where SCL condition is met. The values of R_{max}/λ_D in Fig. 6 are slightly different from the value also given in Ref. 14 because of our use of Eq. (38) for z_2, instead of a further approximation $\Psi_p/z_1^2 = (1 + 2\beta\xi_2)\Psi_p/z_2^2$ as in Eq. (A6) of Ref. 14. Figure 9 shows Ψ/Ψ_p versus $1/z^2$ profiles for $\nu = 100$, and $\Psi_p = 5000$, 1000 and 300. Because the second transitional layer is not actually solved (only the solution behavior being found at both layer ends), this layer is not shown in this figure.

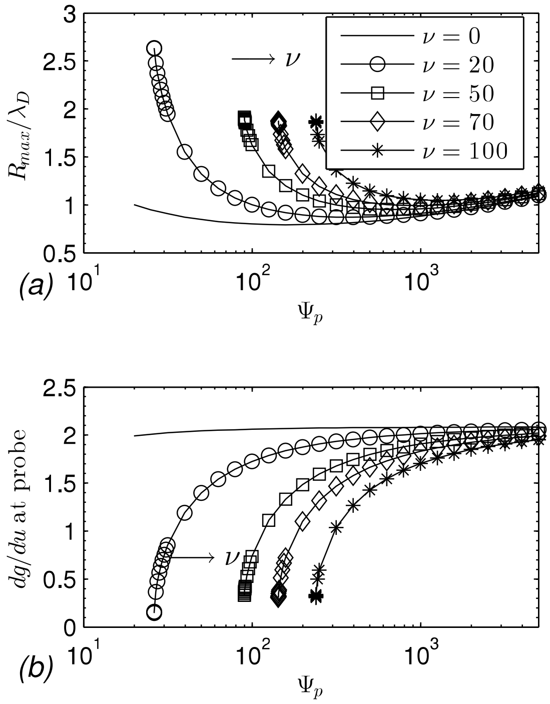

FIG. 6. The maximum radius and the derivative at the probe for $\theta = 4$ and several ν, and for a range of Ψ_p. Except for the case $\nu = 0$, curves end at the probe potential where the SCL condition is met, being $\Psi_{SCL} = 26.2$, 89.7, 143.0 and 238.8 for $\nu = 20$, 50, 70, and 100 respectively.

A. Effects of emitted electrons

For a given Ψ_p, the space charge effect from emitted electrons increases with emission level ν due to more emission from the probe. For a given ν, the effect increases with decreasing Ψ_p. This is because electric field inside the sheath accelerates the electrons less if Ψ_p decreases, which thus results in more space charge everywhere. The influence of ν and Ψ_p on space charge effect is indicated by the parameter μ_s in Eq. (50), shown in Fig. 8d.

As shown by Fig. 6a, thermionic emission clearly increases the range of radius R for OML validity. At very high probe bias, after emitted electrons have been accelerated by the strong electric field, their space charge results in negligible effect throughout the sheath. Therefore, R_{max} is close to its value for no emission and $\mathrm{d}g/\mathrm{d}u|_{z=1}$ changes like an ion sheath without emission. Decrease of Ψ_p or increase of ν in Eq. (50) enlarges μ_s as shown in Figs. 8d, increasing electron space charge effect inside the sheath. For a given level ν, with Ψ_p decreasing, excess of electron space charge reduces the electric field in front of the probe, which decreases sharply when approaching the SCL condition, as shown in Fig. 6b. The more intense the emission is, the higher $\Psi_{SCL}(\nu, \theta)$ is.

We note that for higher emission level ν, more numerical difficulties for locating the exact SCL condition, $\mathrm{d}g/\mathrm{d}u|_{z=1} = 0$, are encountered. This is probably due to increased space charge effect near SCL condition, as compared to lower emission level. Therefore, for higher emission level ν, a small change in Ψ_p renders a greater change in $\mathrm{d}g/\mathrm{d}u|_{z=1}$. We can still determine however the SCL probe potential to five significant figures.

TABLE I. Comparison of probe potential when the SCL condition is met, whether considering (Ψ_{SCL}) or not (Ψ_{SCLn}) the emitted electron density outside the sheath.

	$\nu = 20$	$\nu = 50$	$\nu = 70$	$\nu = 100$
Ψ_{SCL}	26.2	89.7	143.0	238.8
Ψ_{SCLn}	10.1	46.4	81.4	147.9

Figure 9 shows the smooth matching among profile layers. However, we can see that the gap between sheath and first transitional layer increases as Ψ_p decreases, which is also shown as the difference between z_1 and z_2 in Figs.7c and 7d. Given by Eq. (38), the thickness of these two transitional layers increases with β (Fig. 8a), which weakened the validity of the expansions implied in the derivations.

Although the emitted electron density will be negligible far away in the quasineutral region, its effect can not be generally neglected throughout $z > z_2$. To discuss the effects of emitted electrons, we construct the solution which ignores their space charge outside the sheath, thus keeping a given ν value in the sheath attached to the probe, but setting $\nu = 0$ in Eqs. (28), (33) and (A2) for z_0, z_1, Ψ_0, Ψ_1 and μ, and also μ_s in Eq. (51) for the matching between second transitional layer and sheath. As expected from reduced electron space charge, the SCL condition is met at some lower potential (Table I), showing significant difference.

If emitted electrons are considered negligible outside the sheath, the values of z_0, z_1, Ψ_0 and Ψ_1 will be the same as the case of no emission from the probe ($\nu = 0$). This is because, under condition $R = R_{max}$, they do not need information from the sheath. We compare the results of Ψ_0, Ψ_1 and Ψ_p/z_1^2 for each ν to that of $\nu = 0$, Figs. 7a - 7c. For very high potential, changes of ν or Ψ_p cause negligible effects on the results. The error due to the no-emitted-electron-outside approximation increases with Ψ_p decreasing or ν increasing. For the range of parameters we have considered, because $\Psi_{SCL}(\nu = 20)$ is much lower than that for other ν values, a maximum error, around 50% decrease in the values, is found at $\nu = 20$ when the SCL condition is met. Thus the emitted electron density can not always be ignored at z_0 and z_1, leaving alone further closer to the probe. Consequently, a maximum 50% decrease in ξ_{Dm} with no-electron-outside approximation is also found at for $\nu = 20$ and $\Psi_{SCL}(\nu = 20)$. Evaluating the emitted electron density at z_0, $\nu \times n_{em}(z_0)$, shows a maximum density around 0.15 for $\nu = 20$ and $\Psi_{SCL}(\nu = 20)$, being not negligible. In the case of a tether cathodic segment, considering uniform temperature and work function, although the emit-

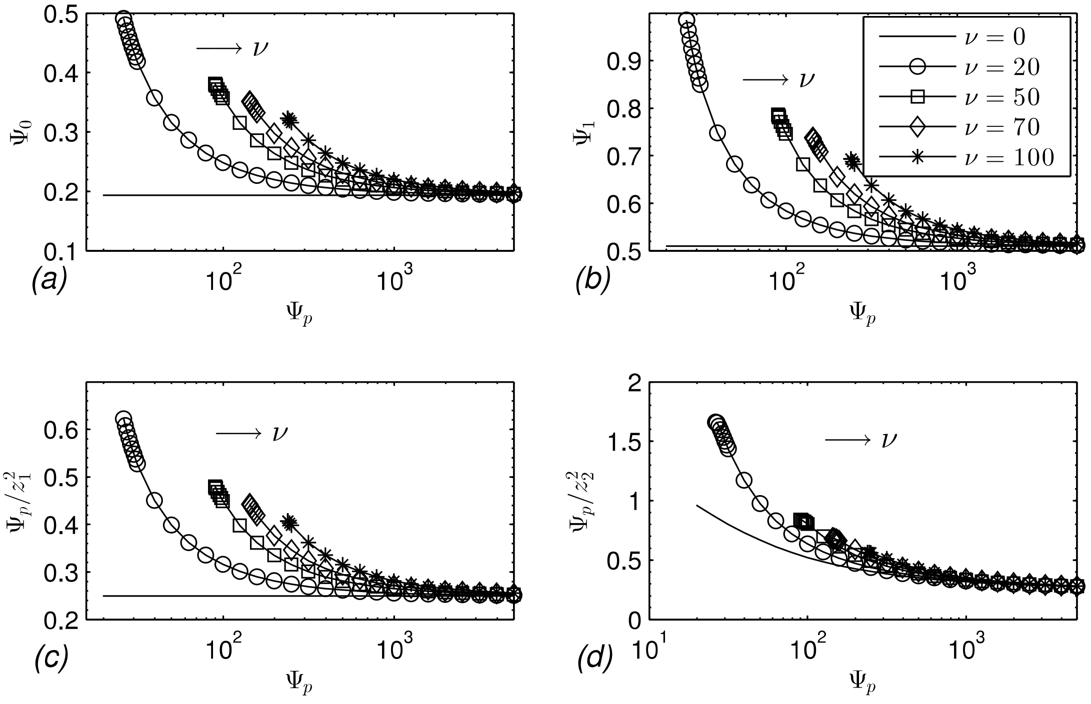

FIG. 7. Ψ_0, Ψ_1, z_1^2/Ψ_p and z_2^2/Ψ_p versus Ψ_p, for $\theta = 4$ and several ν values.

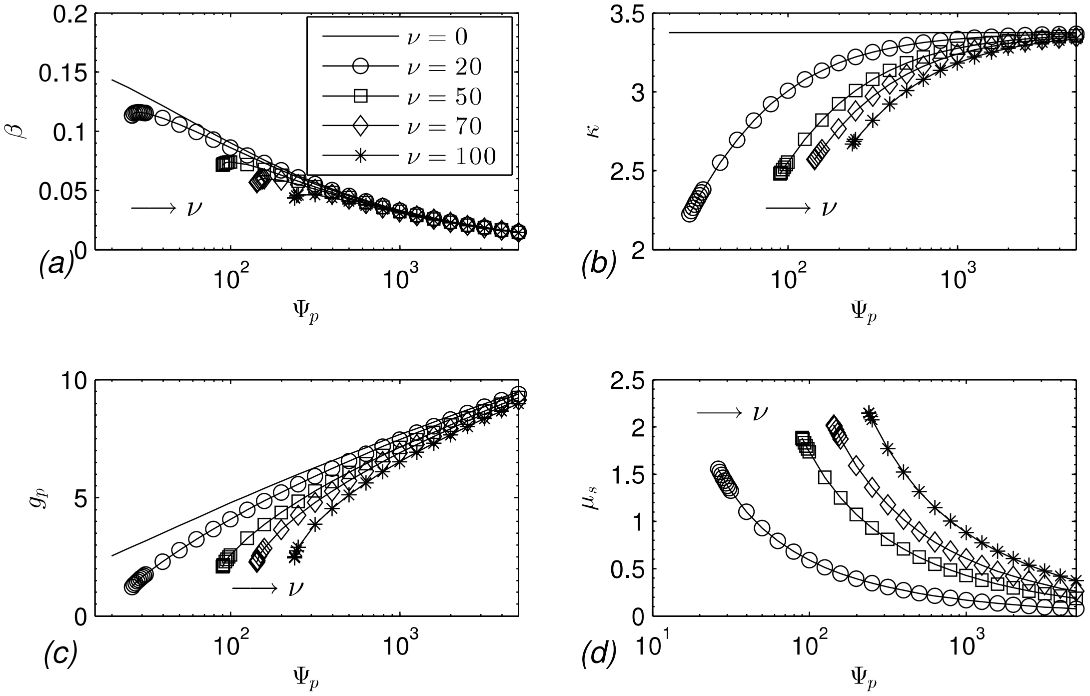

FIG. 8. β, κ, g_p and μ_s versus Ψ_p, for $\theta = 4$ and several ν values.

ted electron density can be safely ignored far below point B* in Fig. 1, it can not near B*.

B. Current

To evaluate the effectiveness of thermionic emission, it is important to compare the RDS thermionic current, Eq. (4), with the respective OML collection current at

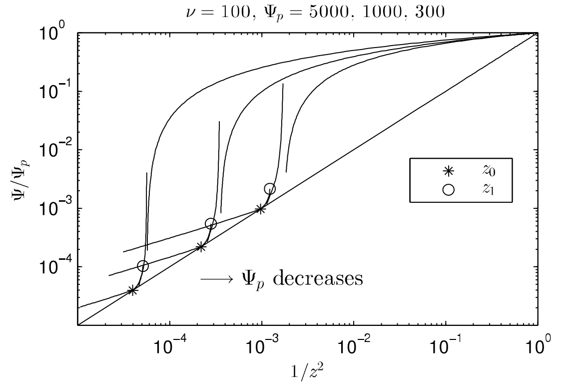

FIG. 9. Potential profiles for $\theta = 4$, $\nu = 100$, and three values of bias Ψ_p.

equal bias $|\Psi_p|$, Eq. (3), the ratio being

$$\sqrt{\frac{m_e}{m_i}}\frac{I_{emp}}{I_{iOML}} = \frac{I_{emp}}{I_{eOML}} = \nu\sqrt{\frac{\pi}{\theta|\Psi_p|}}\ , \qquad (53)$$

with ν and Ψ_p typically large. The ratio I_{emp}/I_{iOML} is much larger than the ratio I_{emp}/I_{eOML} shown in Fig. 10, with a factor of $\sqrt{m_i/m_e} \approx 171$ for oxygen ions. This large ratio clearly shows that thermionic emission is far more efficient than ion OML collection in tether cathodic current exchange. The ratio I_{emp}/I_{eOML} compares the thermionic emission at the cathodic segment to the electron OML collection at the anodic segment for equal bias $|\Psi_p|$. Figure 10 shows that the ratio is of order unity, which suggests that there will be no large disparity in the lengths of the cathodic and anodic segment, making current emission/collection similarly effective in tether applications.

However, although higher emission would undoubtedly emit more current in the no-valley case, the SCL condition is met at higher probe potential (Fig. 6). Thus point B* is moved more towards the cathodic end, leaving longer segment where current is $I_{em} < I_{emp}$. As a result, whether more RDS emission (say lower work function or higher temperature) would always increase the cathodic contact efficiency still needs to be discussed in the analysis of the valley case. The parametric design of a bare-tether system is ambient dependent, with effects of tether temperature due to heating under operation, plasma density, and temperature. The analysis for the valley case will be important to choose the proper length of the coated cathodic segment for each mission.

ACKNOWLEDGMENTS

This work was supported by European Commission FP7 Space Project 262972 (BETs).

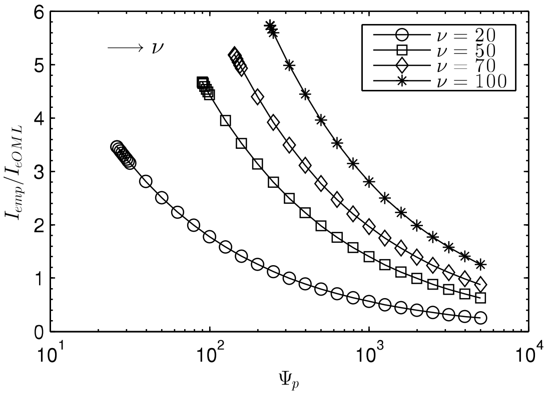

FIG. 10. The emitted electron current compared with OML electron current at same $|\Psi_p|$, $\theta = 4$.

Appendix A: Transitional layer at z_1

Due to the sharp potential increase, the j-line moves to the right from z_1 to z_2, being nearly parallel as shown in Fig. 5, giving $j_z^*(\epsilon) \approx j_{env}(\epsilon)$ for the values $\epsilon = O(1)$ of interest. Thus the ion density will be as in Eq. (31). We can expand the RHS of Poisson's equation about z_1 and Ψ_1, to order $z_1 - z$ and $(\Psi - \Psi_1)^2$, which represents the divergent behavior of quasineutral potential at z_1, $\Psi - \Psi_1 \backsim \sqrt{z_1 - z}$, leading[14]

$$\frac{\mathrm{d}^2\Psi}{\xi_D^2\,\mathrm{d}z^2} = \mu\frac{z_1 - z}{z_1} + \lambda\frac{(\Psi - \Psi_1)^2}{2}, \qquad (A1)$$

where the parameters μ and λ are given by

$$\mu = \int_0^\infty \frac{\exp(-\epsilon)}{\pi} \times \left[2\sqrt{\frac{j_{env}^2(\epsilon)}{j_{z_1}^2(\epsilon) - j_{env}^2(\epsilon)}} - \sqrt{\frac{\Psi_p}{j_{z_1}^2(\epsilon) - (\epsilon + \Psi_p)}}\right] \mathrm{d}\epsilon - \frac{\nu}{z_1\sqrt{\pi\theta\Psi_p}}\ , \qquad (A2)$$

$$\lambda = \int_0^\infty \frac{\exp(-\epsilon)}{4\pi(\epsilon + \Psi_1)^2}\left\{2j_{env}\frac{3j_{z_1}^2(\epsilon) - 2j_{env}^2(\epsilon)}{\left[j_{z_1}^2(\epsilon) - j_{env}^2(\epsilon)\right]^{3/2}} - \sqrt{\Psi_p}\frac{3j_{z_1}^2(\epsilon) - 2(\Psi_p)}{\left[j_{z_1}^2(\epsilon) - (\epsilon + \Psi_p)\right]^{3/2}}\right\} \mathrm{d}\epsilon - \exp(-\Psi_1)\ . \qquad (A3)$$

After defining

$$\frac{z_1 - z}{z_1} = \beta\xi \equiv \left(\sqrt{\frac{2}{\lambda\mu}}\frac{1}{\xi_D^2 z_1^2}\right)^{2/5}\xi\ ,$$

$$\Psi - \Psi_1 = \sqrt{\frac{2\mu\beta}{\lambda}}Y\ , \qquad (A4)$$

Poisson's equation becomes the first Painleve transcendent[27] with initial condition that matches smoothly the quasineutrality solution from z_1 outwards,

$$\frac{\mathrm{d}^2 Y}{\mathrm{d}\xi^2} = Y^2 + \xi \ , \quad \lim_{\xi \to -\infty} -Y = \sqrt{-\xi} \ . \tag{A5}$$

For the expansion to be valid in this thin layer, it is required β to be small, which is validated as in Fig. 8a. Integration shows Y diverging as $\approx 6/(\xi - \xi_2)^2$ at $\xi \to \xi_2 \approx 3.42$, giving z_2 as[11,14]

$$z_2 = z_1 \left(1 - \beta \xi_2\right) \ , \quad \xi_2 \approx 3.42 \ . \tag{A6}$$

This layer is shown in Fig. 2 as the curve passing through the circle markers. It matches well with the solution between z_0 and z_1, and then tends to infinity as a pole at z_2. As Ψ_2 diverges at z_2, is actually left undetermined; neither z_2 nor Ψ_2 are marked in the figures.

[1] J. R. Sanmartin, M. Martinez-Sanchez, and E. Ahedo, J Propul Power **9**, 353–360 (1993).

[2] E. Ahedo and J. R. Sanmartín, J Spacecraft Rocket **39**, 198–205 (2002).

[3] J. R. Sanmartin, E. C. Lorenzini, and M. Martinez-Sanchez, J Spacecraft Rocket **47**, 442–456 (2010).

[4] Y. Toda, S. Matsuishi, K. Hayashi, K. Ueda, T. Kamiya, M. Hirano, and H. Hosono, Adv. Mater. **16**, 685–689 (2004).

[5] S. W. Kim and H. Hosono, Philos. Mag. **92**, 2596–2628 (2012).

[6] Y. Toda, H. Yanagi, E. Ikenaga, J. Kim, M. Kobata, S. Ueda, T. Kamiya, M. Hirano, K. Kobayashi, and H. Hosono, Adv. Mater. **19**, 3564–3569 (2007).

[7] L. Rand, *A Calcium Aluminate Electride Hollow Cathode*, Ph.D. thesis, Colorado State University (2014).

[8] J. Williams, J. Sanmartin, and L. Rand, IEEE Trans. Plasma Sci **40**, 1441–1445 (2012).

[9] X. Chen and J. R. Sanmartin, Phys. Plasmas **19**, 073508 (2012).

[10] I. Bernstein and I. Rabinowitz, Phys. Fluids **2**, 112–121 (1959).

[11] S. Lam, Phys. Fluids **8**, 73 (1965).

[12] E. Ahedo, M. MartinezSanchez, and J. Sanmartin, Phys. Fluids B **4**, 3847–3855 (1992).

[13] J. Laframboise, *Theory of Spherical and Cylindrical Langmuir Probes in a Collisionless, Maxwellian Plasma at Rest*, Ph.D. thesis, University of Toronto (1966).

[14] J. Sanmartin and R. Estes, Phys. Plasmas **6**, 395 (1999).

[15] R. D. Estes and J. R. Sanmartin, Phys. Plasmas **7**, 4320–4325 (2000).

[16] J. Sanmartin, E. Choiniere, B. Gilchrist, J. Ferry, and M. Martinez-Sanchez, IEEE Trans. Plasma Sci **36**, 2851–2858 (2008).

[17] G. Sanchez-Arriaga and J. R. Sanmartín, Phys. Plasmas **19**, 063506 (2012).

[18] M. Charro, J. Sanmartin, C. Bombardelli, A. Sanchez-Torres, E. Lorenzini, H. Garrett, and R. Evans, IEEE Trans. Plasma Sci **40**, 274–281 (2012).

[19] I. Langmuir, Phys. Rev. **33**, 954–989 (1929).

[20] F. W. Crawford and A. B. Cannara, J. Appl. Phys **36**, 3135 – 3141 (1965).

[21] P. D. Prewett and J. E. Allen, Proc. R. Soc. Lond. A. **348**, 435 – 446 (1976).

[22] T. Gyergyek, J. Kovacic1, and M. Cercek, Phys. Plasmas **17**, 083504 (2010).

[23] A. Fruchtman, D. Zoler, and G. Makrinich, Phys. Rev. E **84**, 025402 (2011).

[24] R. Wei and P. J. Wilbur, J. Appl. Phys **60**, 2280–2284 (1986).

[25] K. Chang and G. Bienkowski, Phys. Fluids **13**, 902 (1970).

[26] O. Richardson, *The Emission of Electricity from Hot Bodies* (Longmans Green And Company, 1916).

[27] C. Bender and S. Orszag, *Advanced Mathematical Methods for Scientists and Engineers I: Asymptotic Methods and Perturbation Theory*, Advanced Mathematical Methods for Scientists and Engineers (Springer, 1999).

View publication stats